Optimal Controller Design for Transient Stability Enhancement of Grid-Following Converters Under Weak-Grid Conditions

Taul, Mads Graungaard; Wu, Chao; Chou, Shih-Feng; Blaabjerg, Frede

Published in:
IEEE Transactions on Power Electronics

DOI (link to publication from Publisher):
10.1109/TPEL.2021.3066205

Publication date:
2021

Document Version
Publisher's PDF, also known as Version of record

Optimal Controller Design for Transient Stability Enhancement of Grid-Following Converters Under Weak-Grid Conditions

Mads Graungaard Taul, *Member, IEEE*, Chao Wu, *Member, IEEE*, Shih-Feng Chou, *Member, IEEE*, and Frede Blaabjerg, *Fellow, IEEE*

***Abstract*—Modeling and design-oriented control of transient stability of grid-following converters have attained an increasing interest in recent years. Despite novel nonlinear models enabling a design-oriented enhanced transient stability controller, the focus has so far been limited to study only the synchronization dynamics of the phase-locked loop. To expand upon the knowledge of the large-signal performance and stability, this article proposes a systematic analysis procedure of a grid-following converter under weak-grid conditions and large-signal disturbances including the outer dc-link and ac-side voltage control loops. A reduced-order large-signal model is used to analyze the large-signal nonlinear behavior of the system using the area of the basin of attraction as a measure for large-signal robustness. Here, stabilizing and destabilizing trends for outer-loop controller parameters are given. Through a surrogate-model expensive black-box optimization algorithm, a computational-efficient optimal design of the outer-loop controller parameters is proposed to maximize the large-signal robustness. Finally, a recommendation and a design guideline for converter constraints and outer-loop controller parameters are given. This can be used to identify the influencing parameters for grid-following converters under large-signal disturbances, and as a tool for fast controller optimization toward large-signal robustness.**

***Index Terms*—Grid-connected converters, nonlinear analysis, reduced-order modeling, transient stability.**

I. Introduction

With the rapid increase of power converter-based generation installed in today's and future power systems, the dynamical response of the power system will be significantly different from the conventional synchronous generator-based power system. Unlike synchronous machines, whose transient dynamical response is mainly determined by the physical properties of the machine, the converter dynamical response to disturbances is entirely determined by the employed converter control [1]. This fact has led to an increasing interest and demand for understanding how grid-connected converters act and interact with the grid during large-signal disturbances and weak-grid conditions [2]–[5].

In recent years, a significant amount of research has been conducted to study the transient stability of loss of synchronization of grid-following phase-locked loop (PLL) synchronized converters [4], [6]. This includes enhanced models for transient stability assessment [3], [7]–[12], novel control methods for enhanced transient stability [2], [13]–[21], loss of synchronization analysis under asymmetrical fault conditions [22], and for multiconverter systems [23]–[25]. However, in the abovementioned studies, only the synchronization dynamics of the PLL are considered. This means that the potential stabilizing or destabilizing effects of the outer dc-side voltage controller (DVC) and ac-side voltage controller (AVC) have been overlooked. Accordingly, the impact and interactions from the outer-loop control must be considered for obtaining a more complete picture of the transient stability dynamics of grid-following converters under large-signal disturbances.

The outer-loop interactions have been comprehensively studied for grid-following converters under weak-grid conditions in [26]. However, only the small-signal dynamics are addressed. In [27], the outer loops have been considered and a large-signal reduced-order model is proposed. Anyhow, the impact the outer loops have on the large-signal stability is not disclosed specifically nor fully understood. To that end, grid faults are considered in the analysis where usually the dc-link must be protected by activating dc-side chopper control, which completely alters the converter control and associated model. Also, in [28] and [29], the outer-loop controls are considered during large-signal disturbances. Here, a catastrophic bifurcation is identified for the system under voltage dips and a large-signal stability criterion is proposed for the system. In these works, nonlinear overmodulation of the pulsewidth modulation (PWM) module is found as the origin of instability during large-signal disturbances, but the influence of outer-loop parameters is not of focus. Also, again a voltage sag scenario is considered where the dc-link control will have to protect itself in a practical implementation.

Despite these scattered works, how the outer-loop control affects the large-signal stability and robustness is not well

Manuscript received December 14, 2020; revised February 20, 2021; accepted March 11, 2021. Date of publication March 17, 2021; date of current version June 1, 2021. This work was supported by the Reliable Power Electronics-Based Power System (REPEPS) Project at the Department of Energy Technology, Aalborg University, as a part of the Villum Investigator Program funded by the Villum Foundation. Recommended for publication by Associate Editor M. Su. *(Corresponding author: Chao Wu.)*

The authors are with the Department of Energy Technology, Aalborg University, 9220 Aalborg, Denmark (e-mail: mkg@et.aau.dk; cwu@et.aau.dk; shc@et.aau.dk; fbl@et.aau.dk).

Color versions of one or more figures in this article are available at https://doi.org/10.1109/TPEL.2021.3066205.

Digital Object Identifier 10.1109/TPEL.2021.3066205

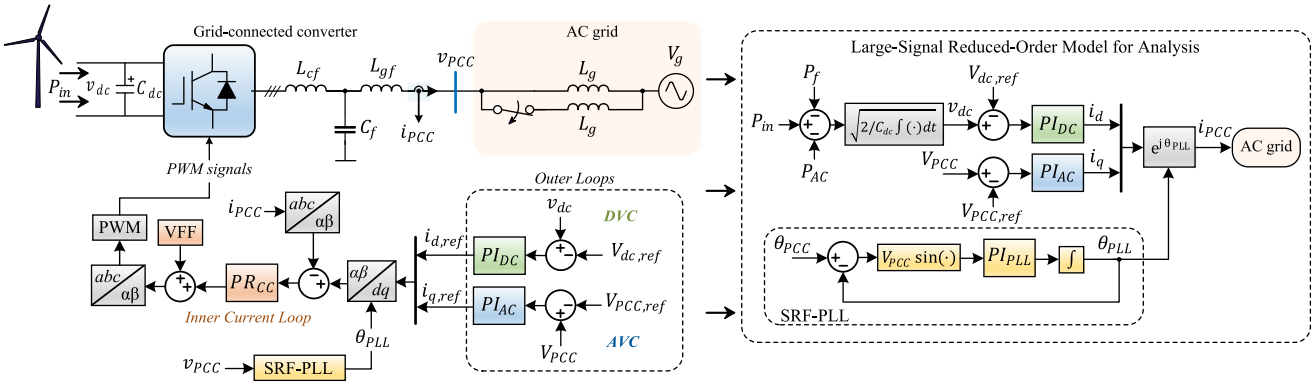

Fig. 1. Structure of grid-connected converter connected to an ac grid. The converter control comprises a grid-following structure with outer direct voltage control (DVC) and alternating voltage control (AVC) where an SRF-PLL is adopted for grid synchronization. The inner-current loop contains a proportional-resonant control with VFF. The ac grid resembles a fault recovery or line contingency case where the effective SCR is increased due to circuit breakers opening a faulted line. The block diagram of a reduced-order large-signal model neglecting the fast inner dynamics is shown in the right, which is used for linear and nonlinear system analysis.

understood. In that connection, an identification of which physical and controller parameters that have a significant influence of the transient stability, and a design guideline for large-signal stability enhancement is missing in prior-art studies.

This article addresses these research gaps by performing a systematic analysis procedure of a grid-following converter under weak-grid conditions and large-signal disturbances. This is done by using a derived reduced-order large-signal model, which is analyzed in the large-signal domain using the area of the basin of attraction (AOT) as a measure for large-signal robustness. Through a surrogate-model expensive black-box optimization algorithm, a computational-efficient optimal design of the outer-loop controller parameters is given, which maximizes the large-signal robustness. Finally, a recommendation and a design guideline for converter constraints and outer-loop controller parameters are given. This can be used for enhanced understanding of the influencing parameters for grid-following converters under large-signal disturbances, and as a tool for fast controller optimization for maximizing the large-signal robustness.

The remainder of this article is structured as follows. In Section II, the system under study is presented and the nonlinear model used for system analysis is detailed. A comprehensive large-signal analysis is conducted in Section III where trend analysis is obtained between controller parameter variations and the nonlinear basin of attraction of the system. The highlighted trends are also verified using a detailed simulation model. Based on the stability trend analysis of the outer-loop controller parameters, an surrogate-model expensive black-box optimization algorithm is employed in Section IV to find the optimal controller parameter set such to maximize the large-signal robustness of the grid-following converter. Subsequently, a design guideline and recommendation for controller parameter selection are given in Section V. The obtained findings are experimentally verified in Section VI. Finally, this article is concluded in Section VII.

II. Nonlinear Model Development

A typical grid-connected converter transferring harvested renewable energy from, e.g., a wind turbine to the grid is considered for this analysis, as shown in Fig. 1. In order to guarantee the machine-side converter to achieve the maximum power point tracking, the dc-link voltage is controlled by the grid-side converter, as shown Fig. 1. For other outer-loop control methods such as active power control and reactive power control, this will be addressed in future work. It uses a grid-following control structure where the dq-axes current references are oriented to the control frame determined by the synchronous-reference frame phase-locked loop (SRF-PLL). The outer loops include a dc-link voltage controller (DVC) for maintaining a constant dc-link voltage and an ac-side voltage controller (AVC) for regulating the level of the point of common coupling (PCC) voltage. The voltage feed-forward (VFF) includes active damping of the filter resonance as proposed in [30]. The grid-following converter is connected to an inductive ac grid where a high-impedance condition, caused by a redundant line being forced open during a contingency, is analyzed. This represents a topological change where, for example, a short-circuit condition is eliminated by quickly disconnecting the faulted line, which could cause a sudden short-circuit ratio (SCR) change. Control and system parameters for Fig. 1 are listed in Table I. The base-line design shown for the controller parameters in Table I is based on typical design parameters with a PLL bandwidth of 30 Hz, a dc-link controller bandwidth of 10 Hz, and the AVC parameters as employed in [27].

Large-signal synchronization stability or transient instability of grid-tied units is often described as an active power transfer problem. Therefore, the static influence of the outer-loop control on the transferable active power is first analyzed.

A. Influence of Outer-Loop Controls on Transferable Power

During steady state, $v_q = 0$ and $\theta_{\text{PLL}} = \theta_{\text{PCC}} = \sin^{-1}(X_g i_d / V_g)$, where X_g is the grid impedance. Using

TABLE I
CONTROL AND SYSTEM PARAMETERS

Symbol	Description	Value
V_b	Nominal grid voltage (line-line, rms)	690 V
V_g	Grid voltage (line-line, rms)	690 V
P_{in}	Nominal power	3.6 MVA
f_0	Rated frequency	50 Hz
L_g	Grid inductance	0.5 pu
f_{sw}	Switching frequency	2.5 kHz
L_{cf}	Converter-side filter inductor	0.12 pu
R_f	Filter equivalent resistance	2 mΩ
L_{gf}	Grid-side filter inductor	0 pu
C_f	Filter capacitor	2 mF
C_{dc}	dc-link capacitor	180 mF
$V_{dc,ref}$	dc-link voltage reference	1250 V
$V_{PCC,ref}$	PCC voltage reference	V_g
K_{pc}	Current controller K_p	0.0793 Ω
K_{rc}	Current controller K_r	12.46 Ω/s
$K_{p,PLL0}$	Base-line PLL Design of K_p	0.2259 rad/(V s)
$K_{i,PLL0}$	Base-line PLL Design of K_i	14.38 rad/(V s^2)
$K_{p,DC0}$	Base-line DVC Design of K_p	25.09 Ω^{-1}
$K_{i,DC0}$	Base-line DVC Design of K_i	321.20 Ω^{-1}/s
$K_{p,AC0}$	Base-line AVC Design of K_p	1 Ω^{-1}
$K_{i,AC0}$	Base-line AVC Design of K_i	100 Ω^{-1}/s

this, then the active power at the ac-side can be expressed as

$$P_{\text{AC}} = \frac{3}{2} i_d \left(V_g \sqrt{1 - \left(\frac{X_g i_d}{V_g} \right)^2} - X_g i_q \right). \tag{1}$$

Here, i_q is determined using the AVC control, which can clearly participate in improving the active power transfer. By considering converter current limitation, two possible relationships for the ac-side active power can be formulated as shown in (2) as shown at the bottom of this page—one where the converter current limitation is not exceeded by i_d and i_q, and one where current limitation is met and the reactive current is limited accordingly. With these formulations, the effect of the AVC control on the power transfer capability of the grid-connected converter can be analyzed.

The output active power versus the d-axis current for the converter without and with AVC is shown in Fig. 2(a) for an SCR = 2. The required q-axis current without and with the AVC is shown in Fig. 2(b). Note that during this weak-grid condition, satisfying a 1 p.u. input power and requires a large injection of i_d without using the AVC to support the PCC voltage. Actually the current magnitude needed for transferring 1 p.u. of active current without AVC is 1.4 p.u., whereas the current magnitude needed with the AVC is only 1.03 p.u. Therefore, this clearly highlights the benefits of using the AVC during weak-grid conditions to support the point of connection voltages. Also, during large-signal disturbances, instability may occur due to the oscillations and imbalances between input power and transferred

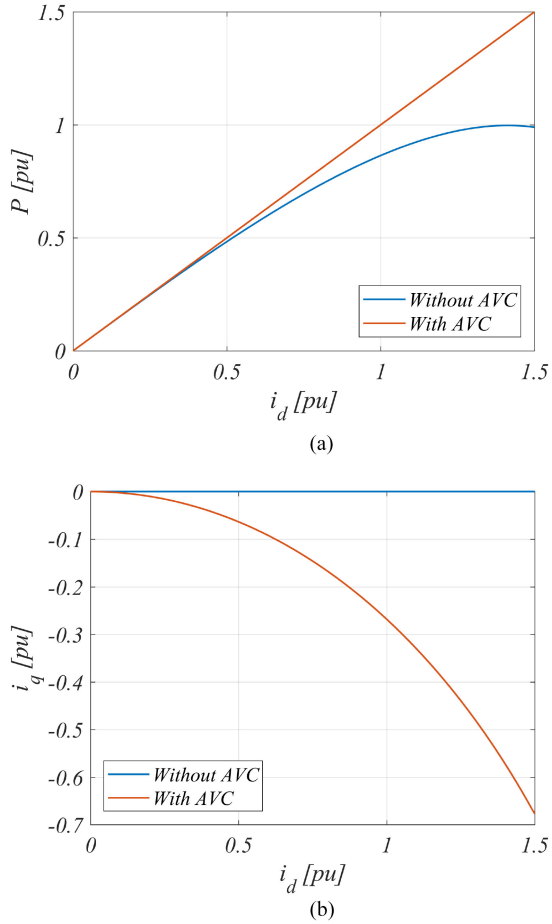

Fig. 2. Converter output active power and reactive current injection without and with AVC for SCR = 2 using (2).

output power. During such conditions, it can be anticipated from Fig. 2 that a tightly regulated AVC will have a stabilizing effect on the overall response.

As disclosed earlier, the PCC voltage magnitude, which in steady state is regulated from the AVC, has a large impact on the transferable power. According to Fig. 1, the PCC voltage can be written as

$$\boldsymbol{v}_{\text{PCC}} = V_g + jX_g(i_d + ji_q)(\cos(\theta_{\text{PLL}}) + j\sin(\theta_{\text{PLL}})) \tag{3}$$

and its magnitude as

$$V_{\text{PCC}} = \sqrt{V_g^2 - 2V_g X_g (i_q \cos(\theta_{\text{PLL}}) + i_d \sin(\theta_{\text{PLL}})) + X_g^2 (i_d^2 + i_q^2)}. \tag{4}$$

$$P_{\text{AC}} = \begin{cases} \frac{3}{2} V_g i_d & \text{if } I_{\text{lim}} > \sqrt{i_d^2 + i_{q1}^2} \quad \text{where} \quad i_{q1} = \frac{V_g}{X_g} \left(\sqrt{1 - \left(\frac{X_g i_d}{V_g} \right)^2} - 1 \right) \\ \frac{3}{2} i_d \left(V_g \sqrt{1 - \left(\frac{X_g i_d}{V_g} \right)^2} - X_g i_q \right) & \text{otherwise, } i_q = \sqrt{I_{\text{lim}}^2 - i_d^2} \end{cases} \tag{2}$$

As can be seen from (4), the PCC voltage magnitude is actually a complicated variable influenced by and coupled with all outer control loops. Therefore, the AVC is not only responsible for changes in V_{PCC}, but the dynamics of the DVC and PLL have an impact as well.

From this analysis, it is clear that the outer loops have a significant impact on the transferable power. However, the control dynamics of the loops have also a large effect on whether a static necessary stability condition can be reached or not. For example, current references set by the outer loops may not provide a beneficial response if the PLL aligning these with the PCC voltage frame is too slow. Similarly, if the dynamics of the outer loops do not provide the needed references in due time, instability may also arise despite a sufficiently fast PLL. Therefore, it is a complex system where the combined dynamical responses need to be considered to assess the system stability. Thus, the influence of the DVC, AVC, and PLL must be understood under large-signal disturbances.

To accomplish this, an averaged large-signal reduced-order model is developed. The large-signal model is described in Section II-B and is largely based on what is recently proposed in [27]. One key difference between the models is that the parasitic filter resistance (R_f), which has a large influence on the stability prediction around the stability boundary, is included in this article. Furthermore, this article aims to exploit this model for thorough analysis and to shed light on the complex transient dynamics of the system shown in Fig. 1.

B. Large-Signal Reduced-Order Model

For the large-signal reduced-order model, the effects of the PWM operation and the fast inner current controller are neglected. This assumption can be justified by the large time-scale difference between the outer transient stability dynamics and the inner converter control. Accordingly, it is assumed that the output current of the converter perfectly tracks the commanded references as $i_d = i_{d,\text{ref}}$ and $i_q = i_{q,\text{ref}}$ and that the transient stability dynamics can be characterized by the slow dynamics of the outer loops. The state equations for the outer-loop control, relating the dc-link voltage and ac-side voltage with the d-axis and q-axis current, respectively, are

$$\dot{i}_d = K_{p,\text{DC}}\dot{v}_{\text{dc}} + K_{i,\text{DC}}\left(v_{\text{dc}} - V_{\text{dc,ref}}\right) \tag{5}$$

$$\dot{i}_q = K_{p,\text{AC}}\dot{V}_{\text{PCC}} + K_{i,\text{AC}}\left(V_{\text{PCC}} - V_{\text{PCC,ref}}\right). \tag{6}$$

The dc-link dynamics are governed by the active power balance between the dc and ac side as

$$\frac{C_{\text{dc}}}{2}\frac{d(v_{\text{dc}}^2)}{dt} = P_{\text{in}} - P_{\text{AC}} - P_f. \tag{7}$$

Thereby, the state equation for the dc-link dynamic is

$$\dot{v}_{\text{dc}} = \frac{P_{\text{in}} - P_{\text{AC}} - P_f}{C_{\text{dc}}v_{\text{dc}}} \tag{8}$$

where

$$P_{\text{AC}} = \frac{3}{2}\frac{V_{\text{PCC}}V_g}{X_g}\sin(\theta_{\text{PCC}}) \tag{9}$$

$$P_f = \frac{3}{2}(i_d^2 + i_q^2)R_f \tag{10}$$

where the phase angle is expressed in the reference frame of the grid voltage, i.e., $\theta_g = 0$, V_{PCC}, V_g denote the phase-voltage magnitudes, and R_f is the filter equivalent series resistance. The PCC voltage expressed in the rotating frame of the grid voltage and PLL rotating frame, respectively, are

$$V_{\text{PCC}}e^{j\theta_{\text{PCC}}} = V_g + jX_g(i_d + ji_q)e^{j\theta_{\text{PLL}}} \tag{11}$$

$$\downarrow$$

$$V_{\text{PCC}}e^{j(\theta_{\text{PCC}}-\theta_{\text{PLL}})} = V_g e^{-j\theta_{\text{PLL}}} + jX_g(i_d + ji_q). \tag{12}$$

Here, the PLL estimated frequency is assumed not to deviate much from the nominal frequency, i.e., the grid impedance is assumed constant during the analysis. Thereby, the dq components of the PCC voltage relative to the PLL frame are

$$v_d = V_g\cos(\theta_{\text{PLL}}) - X_g i_q \tag{13}$$

$$v_q = -V_g\sin(\theta_{\text{PLL}}) + X_g i_d \tag{14}$$

and the state equations become

$$\dot{v}_d = -V_g\dot{\theta}_{\text{PLL}}\sin(\theta_{\text{PLL}}) - X_g\dot{i}_q \tag{15}$$

$$\dot{v}_q = -V_g\dot{\theta}_{\text{PLL}}\cos(\theta_{\text{PLL}}) + X_g\dot{i}_d. \tag{16}$$

By introducing an internal state variable of the PLL (integrator state in the PLL PI controller), the PLL phase angle can be expressed as

$$\dot{\theta}_{\text{PLL}} = K_{p,\text{PLL}}\dot{x}_{\text{PLL}} + K_{i,\text{PLL}}x_{\text{PLL}} \tag{17}$$

$$\dot{x}_{\text{PLL}} = v_q = -V_g\sin(\theta_{\text{PLL}}) + X_g i_d. \tag{18}$$

For the PCC dynamics used for the AVC and the expression for P_{AC}, these are given as

$$V_{\text{PCC}} = \sqrt{v_d^2 + v_q^2} \tag{19}$$

$$\downarrow$$

$$\dot{V}_{\text{PCC}} = \frac{v_d\dot{v}_d + v_q\dot{v}_q}{V_{\text{PCC}}} \tag{20}$$

and

$$\theta_{\text{PCC}} = \tan^{-1}\left(\frac{v_q}{v_d}\right) + \theta_{\text{PLL}} \tag{21}$$

$$\downarrow$$

$$\dot{\theta}_{\text{PCC}} = \frac{v_d\dot{v}_q - v_q\dot{v}_d}{V_{\text{PCC}}^2} + \dot{\theta}_{\text{PLL}}. \tag{22}$$

Eliminating the redundant variables (i_d, i_q, v_d, v_q) by using

$$v_d = V_{\text{PCC}}\cos(\theta_{\text{PCC}} - \theta_{\text{PLL}}) \tag{23}$$

$$v_q = V_{\text{PCC}}\sin(\theta_{\text{PCC}} - \theta_{\text{PLL}}) \tag{24}$$

$$i_d = \frac{V_g\sin(\theta_{\text{PLL}}) + v_q}{X_g} \tag{25}$$

$$i_q = \frac{V_g\cos(\theta_{\text{PLL}}) - v_d}{X_g} \tag{26}$$

the fifth-order state-space model of the nonlinear system ($\dot{\boldsymbol{x}} = \boldsymbol{f}(\boldsymbol{x}, t)$) can be expressed as given in (31) shown in the subsequent sections with the fixed-points of (32) shown in the subsequent sections where $\boldsymbol{x}$ is the state vector given as $\boldsymbol{x} = [V_{\text{PCC}}\ \theta_{\text{PCC}}\ v_{\text{dc}}\ \theta_{\text{PLL}}\ x_{\text{PLL}}]^T$.

III. Large-Signal Analysis

Based on the nonlinear model given in (31), both the small-signal and large-signal analysis can be conducted. And the small-signal stability is a precondition of large-signal stability, the detailed relationship between small-signal stability and large-signal stability can be seen in [21]. Since the small-signal stability analysis has been analyzed in [27], it is not repeated in this article. Thus, the focus of this article is to design the parameters based on the large-signal analysis. With the nonlinear model being developed, the influence of the outer loops is to be analyzed from a large-signal perspective.

A. Initial Conditions for Nonlinear Disturbed Model

For proper large-signal analysis, one must assign correct initial conditions to the state variables at the instant of the disturbance. Since a disturbance will immediately affect the PCC voltage, the initial conditions when the disturbance occurs will not equal the fixed points in (32). Since v_{dc}, θ_{PLL}, and x_{PLL} are all located behind an integrator, their initial values cannot jump at the instant of the disturbance. However, for V_{PCC} and θ_{PCC}, this is not the case. For the AVC, i_q will discontinuously jump at the fault instant due to a change in V_{PCC}. However, at the same time, the initial condition for V_{PCC} is also dependent on the injection of i_q. Therefore, this represents an coupled set of equations, whose explicit solution is long and complex. To avoid presenting this expression here, the solution is instead obtained iteratively as follows.

First, the initial value for i_d is calculated as

$$i_{d,0} = \frac{-V_g + \sqrt{V_g^2 - (2R_f i_{q,\text{PF}})^2 + \frac{8}{3}P_{\text{in}}R_f}}{2R_f} \tag{27}$$

which is found from the power balance in (7) with $P_{\text{AC}} = 3/2 i_d V_g$ as

$$\frac{3}{2}i_{d,0}V_g = P_{\text{in}} - \frac{3}{2}R_f(i_{d,0}^2 + i_{q,\text{PF}}^2) \tag{28}$$

where P_{in} is equal to 1 p.u. and the prefault q-axis current can be expressed as

$$i_{q,\text{PF}} = \frac{V_g(\cos(\theta_0) - 1)}{X_g}. \tag{29}$$

Then, the iterative process is computed as follows:

1) $i_{q,0} = i_{q,\text{PF}} + K_{p,\text{AC}}(V_{\text{PCC},0} - V_g)$;
2) $v_{d,0} = V_g\cos(\theta_0) - i_{q,0}X_{g,F}$;
3) $v_{q,0} = -V_g\sin(\theta_0) - i_{d,0}X_{g,F}$;
4) $V_{\text{PCC},0} = \sqrt{v_{d,0}^2 + v_{q,0}^2}$;
5) repeat 1)–4) until changes in initial values are negligible;
6) $\theta_{\text{PCC},0} = \tan^{-1}(\frac{v_{q,0}}{v_{d,0}}) + \theta_0$.

$X_{g,F}$ denotes the total grid reactance during the loss of a redundant line contingency. With this, all initial conditions are determined and the nonlinear model in (31) can be analyzed.

B. Parameter Variation and Basin of Attraction

To analyze the large-signal stability trends of the nonlinear system in (31), a quantitative analysis is performed with a large number of simulation runs. Notably, the system is represented as a fifth-order nonlinear model, whose basin of attraction is also five-dimensional. For the sake of visualization and considering disturbances to occur in the grid voltage, a two-dimensional projection of the full-dimensional space on to the $V_{\text{PCC}} - \theta_{\text{PCC}}$ plane is made in the analysis for this article. For a complete analysis, the optimization can be extended to disturbances in the other parameters as well. For the analysis, one control parameter is varied compared to Table I and the large-signal trajectory is computed for 3600 different initial conditions. If the system dynamical trajectory for a selected initial condition gets attracted to a stable fixed point after the disturbance, the system is stable and that initial condition is said to belong to the basin of attraction. The fixed point of attraction for this analysis is for SCR $= 2$ at the point $V_{\text{PCC}} = 1$ p.u. and $\theta_{\text{PCC}} = 30^\circ$. The basin of attraction is calculated for variation in the AVC controller parameters in Fig. 3. It is evident that $K_{p,\text{AC}}$ has a negligible effect on the basin of attraction, whereas it can be significantly increased in all directions by increasing $K_{i,\text{AC}}$. When looking at the basin of attraction for the DVC in Fig. 4, it is observed that increasing $K_{p,\text{DC}}$ and decreasing $K_{i,\text{DC}}$ increases the attraction area. However, as can be seen from the reverse variation plots, the attraction area is not extended in all directions but it is actually reduced in more areas. The same trend is seen for the variation of $K_{p,\text{PLL}}$ in Fig. 5(a) and (b), whereas a reduction in $K_{i,\text{PLL}}$ increases the attraction area in all directions as seen in Fig. 5(c). Reducing the PLL integral gain for enhanced transient stability is well-known from prior art studies as analyzed and proposed in [4], [6], [13], [17], and [21]. However, in addition to the stability enhancement of the PLL integral gain, several new insights can be extracted from this analysis.

1) Increasing $K_{p,\text{PLL}}$ has from prior-art studies been concluded to be as effective as decreasing $K_{i,\text{PLL}}$ for achieving increased system damping for PLL-synchronized converters. However, as it can be seen in Fig. 5(a) and (b), the stability is only enhanced in some areas for variations in $K_{p,\text{PLL}}$. Thus, reducing the PLL integral gain is a better solution for enhancing the transient stability using the PLL control.
2) Increasing $K_{p,\text{DC}}$ and decreasing $K_{i,\text{DC}}$ in the DVC are mostly beneficial to enlarge the basin of attraction. However, the attraction area is not extended in all directions, which makes a recommendation case specific.
3) Variation in $K_{p,\text{AC}}$ has a negligible effect on the attraction area. However, increasing $K_{i,\text{AC}}$ has a large positive impact on the attraction area in all directions. Therefore, variation on $K_{i,\text{AC}}$ seems as a promising strategy for enhancing the transient stability.

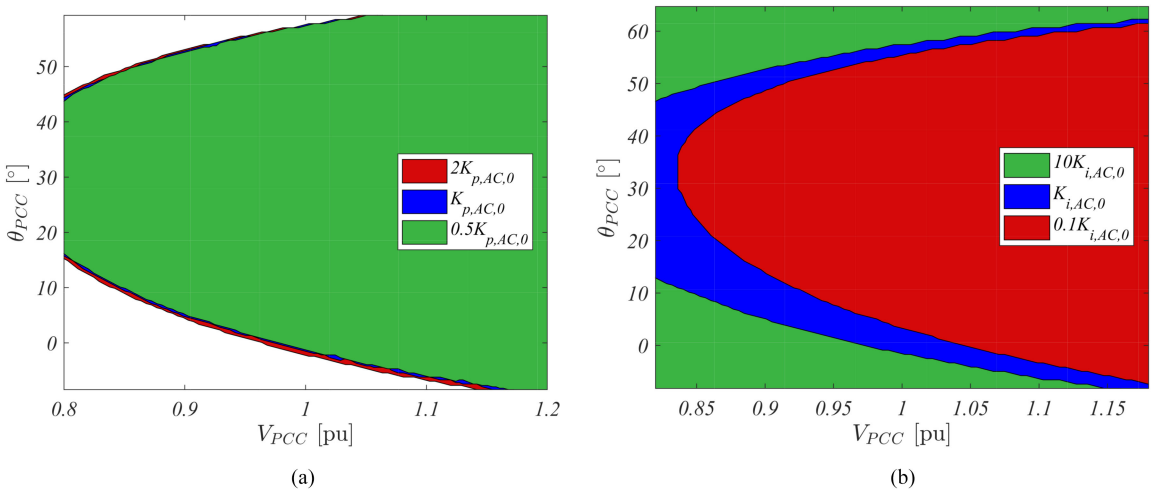

Fig. 3. Basins of attraction for variation in AVC controller parameters for SCR = 2. Only one parameter is varied at a time and the remaining parameters are as listed in Table I. The basin of attraction is the set of initial conditions in the ($V_{\text{PCC}} - \theta_{\text{PCC}}$) plane from where the dynamical system trajectories are able to be attracted to the stable operating point after the disturbance.

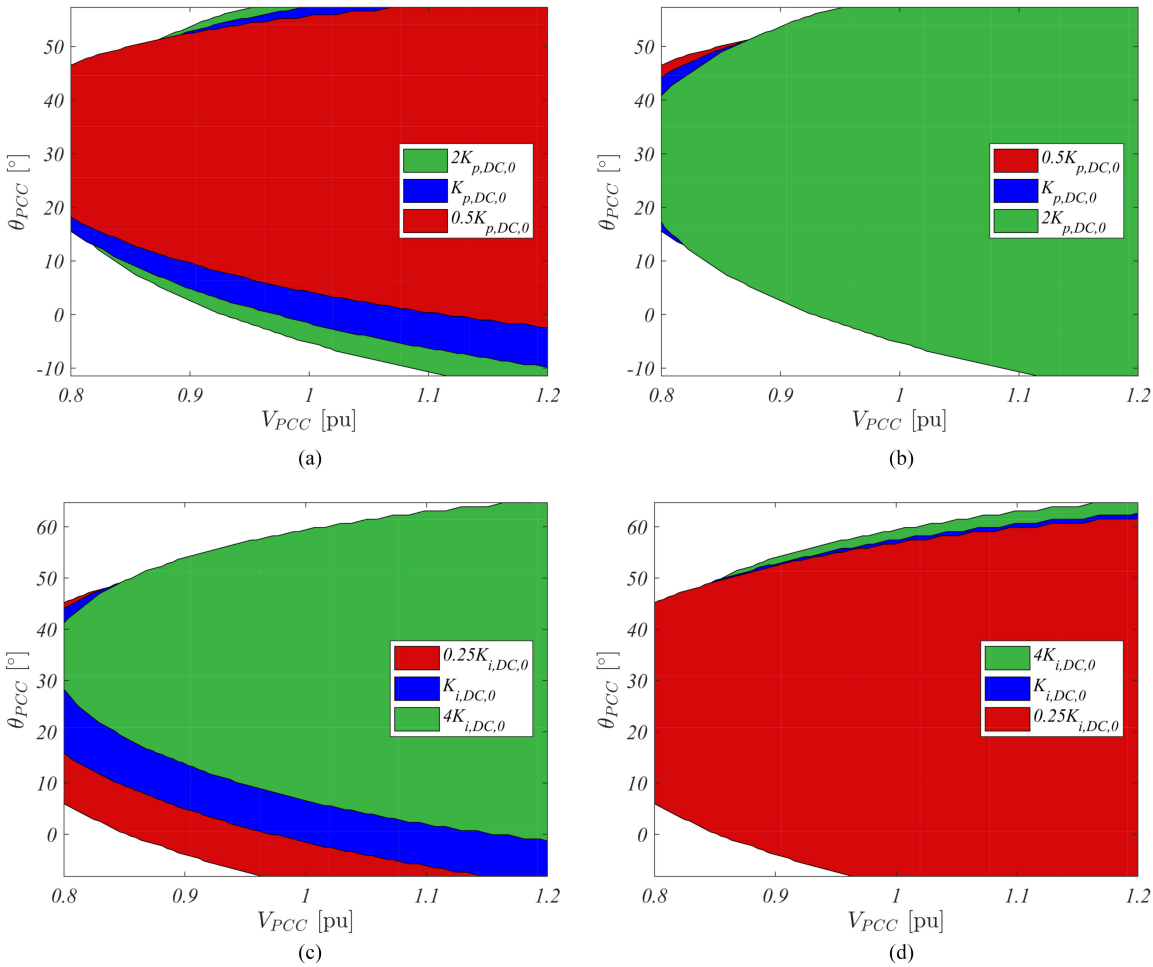

Fig. 4. Basins of attraction for variation in DVC controller parameters for SCR = 2. Only one parameter is varied at a time and the remaining parameters are as listed in Table I.

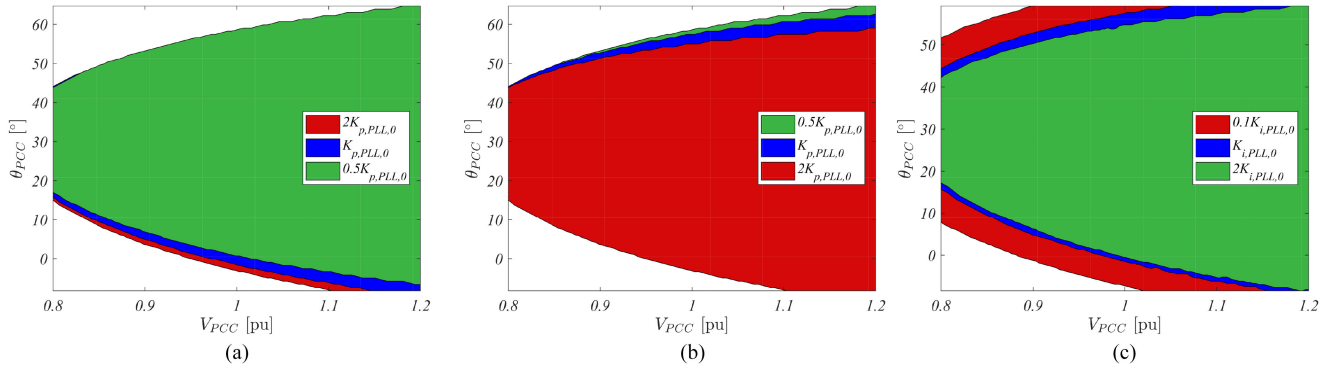

Fig. 5. Basins of attraction for variation in PLL controller parameters for SCR $= 2$. Only one parameter is varied at a time and the remaining parameters are as listed in Table I.

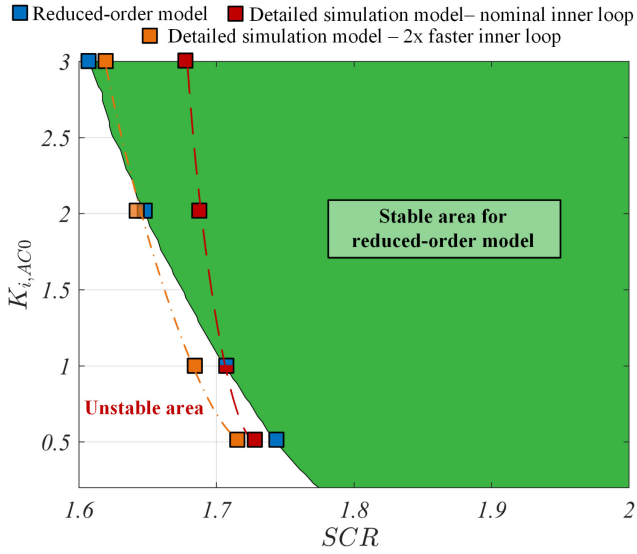

Fig. 6. Stable area of reduced-order large-signal model (31) with a drop in SCR to 1.6–2 from SCR $= 4$ for varying $K_{i,\mathrm{AC}}$. Four points for comparison on the stability boarder are indicated for the reduced-order model and the detailed simulation model with nominal and twice the bandwidth for the inner control loop.

C. Verification of Analysis

The stability assessment using the large-signal reduced-order model from (31) is performed with a varying drop in SCR from SCR $= 4$ and with different control values for $K_{i,\mathrm{AC}}$, as shown in Fig. 6. Additionally, the stability border for the SCR drop for different values of $K_{i,\mathrm{AC}}$ is indicated when using the detailed simulation switching model. For the reduced-order model, the solid line represents the stable boundary and the right side is the stable area, which is filled with the green color. The red dashed line represents the stability boundary of the detailed simulation model with a nominal inner loop. The brown dot-dashed line represents the stability boundary of the detailed simulation model with two times faster inner loop. As can be seen from these three stability borders, the faster inner loop can expand the stable area for the detailed simulation model, which means that a faster inner loop is better for transient stability. By comparing the reduced-order model and the detailed simulation model with a nominal inner loop, the required $K_{i,\mathrm{AC}}$ is larger for the simulation model when the SCR ≤ 1.7. Accordingly, the reduced-order model is seen to overestimate the stability margin in that area. However, for SCR ≥ 1.7, the stability border of the reduced-order model is on the right side of the detailed simulation model, which indicates a tendency to underestimate the stability margin. This is advantageous for real application since it allows for some headroom toward unmodeled dynamics and parameter uncertainties.

This occurs, since the coupling between the outer AVC starts to affect the high-frequency stability including the inner current control, *LCL* filter, and active damping VFF. This effect is clearly demonstrated from the detailed simulation model in Fig. 6 where the bandwidth of the inner loop is doubled. Here, the reduced-order model provides a highly accurate measure of the stability due to the time-scale decoupling between inner and outer loops—also for higher $K_{i,\mathrm{AC}}$. To that end, it is observed from simulation results that the value of active damping has a significant impact on the location of the stability boundary. Accordingly, increasing $K_{i,\mathrm{AC}}$ can indeed increase the stability margin, but the neglect of the inner current dynamics may not be justified for a very high $K_{i,\mathrm{AC}}$ or when the *LCL* filter is weakly damping.

Another important influence of the converter instability happens due to converter saturation, which must be considered in a practical setup, e.g., with a high $K_{i,\mathrm{AC}}$ and a low SCR, the needed converter current to attain stability may violate its maximum limits during the disturbance. This is demonstrated in Fig. 7 where the maximum converter current during a stable response is shown. It is clear that when the SCR drops below 1.8 where the required converter current increases, and a large $K_{i,\mathrm{AC}}$ is needed for stability. Therefore, from a practical point of view, the limitation in converter current, even short-time, needs to be considered. Evaluating a second constraint, the maximum utilization of the dc-link voltage for establishing the ac-side voltage is shown in Fig. 8 for the stable trajectories in Fig. 6. Similarly as what is seen for the maximum current in Fig. 7, the converter constraints are as well being violated around the

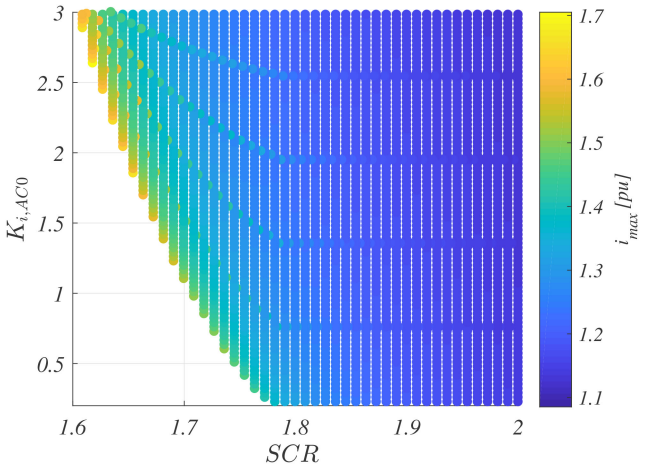

Fig. 7. Value of maximum instantaneous converter current for each stable trajectory from the stable area shown in Fig. 6.

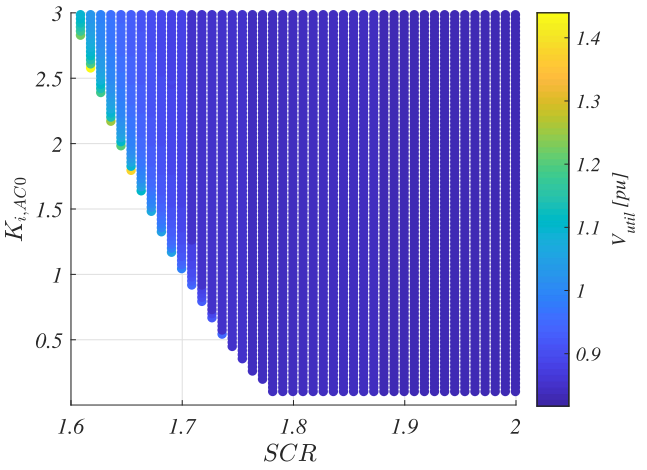

Fig. 8. Value of maximum utilized dc-link voltage, $V_{\text{util}} = \max(V_{\text{PCC}}/(0.5v_{\text{dc}}))$, for each stable trajectory from the stable area shown in Fig. 6.

stability boundary for the voltage utilization. However, considering a drop to SCR ≥ 1.8, the maximum ac-side voltage does not violate the dc-link voltage.

D. Trends in Outer-Loop Control During Large-Signal Disturbances

From the large-signal analysis, it is shown that decreasing $K_{i,\text{PLL}}$ and increasing $K_{i,\text{AC}}$ are the only two trends that extend the basin of attraction in all directions. To that end, as it is seen from Fig. 4, it is generally better for the transient stability to increase $K_{p,\text{DC}}$ and decrease $K_{i,\text{DC}}$. However, this should be done with caution since the large-signal robustness is not extended in all directions. Additionally, it is concluded that the effects of $K_{p,\text{AC}}$ and $K_{p,\text{PLL}}$ are insignificant, which is the reason they are not considered in the following.

Therefore, to improve the transient stability under weak-grid conditions, where a redundant line may be temporarily disconnected, one can under the constraints of the converter apply gain scheduling controller in the following order:

1) increase $K_{i,\text{AC}}$;
2) decrease $K_{i,\text{PLL}}$;
3) decrease $K_{i,\text{DC}}$;
4) increase $K_{p,\text{DC}}$.

Despite these trends being useful for a better system behavior understanding, it does not answer which values among all four controller parameters will provide the largest area of attraction or largest large-signal robustness. This question is key in proposing an effective enhanced design strategy, and it is addressed in the following section using optimization. As will be shown in the following section, the scheduled controller gains as proposed earlier show the same trend for vastly different selections of controller designs. Therefore, the conclusion shown here is not limited only to the baseline parameters from Table I.

IV. Enhanced Transient Stability Through Optimized Outer-Loop Design

For each basin of attraction 3600 different initial conditions are evaluated. Despite the low computational burden of the reduced-order model where each simulation only takes a few milliseconds, it takes around 15 s to compute one basin of attraction plot. Even though this is a rather short time, this is problematic when it is desired to find an optimized selection of controller parameters such to maximize the area of the basin of attraction (AOT), e.g., with the four controller parameters selected, just performing a course grid search with ten values for each controller parameter will take around 42 h to compute. This computational burden is indeed unacceptable and provides no guarantee of an optimal set of point. To avoid this brute-force approach, a black-box optimization algorithm is employed in this article. Since the evaluation of the basin of attraction area involves solving 3600 different simulations, identifying, and keeping the stable operating points, and then computing the area that these points belong to, involves several complicated nonlinear steps, an analytical function cannot be used for the optimization objective function. Therefore, this problem is better to be solved using black-box optimization where the objective function is considered as unknown. Since it is not feasible to run the objective function (compute AOT) many times due to the high computational burden, this falls into the field of expensive black-box optimization where it is desired to find an optimal solution with a minimum number of function evaluations. The optimization problem is defined as a minimization problem of

$$\min g(\boldsymbol{h}) \tag{30}$$

where g is the computational expensive black-box function for the AOT evaluation subject to a box-constrained set of continuous controller parameters $\boldsymbol{h} = [K_{p,\text{DC}}, K_{i,\text{DC}}, K_{i,\text{PLL}}, K_{i,\text{AC}}]$. Other methods including genetic algorithms and particle swarm

methods can be used for black-box optimization. However, because such methods need significantly more function evaluations compared to a surrogate-model approach [31], this approach is utilized here. The basic principle of the surrogate model black-box optimization algorithm can be understood from the flow chart shown in Fig. 9.

First, an initial design set is selected from the parameter space, $\boldsymbol{h}$. This is done using a latin hypercupe sampling strategy, which is a statistical method for selecting an almost random sample set from a multidimensional parameter distribution.

Second, the expensive black-box model is evaluated at these initial points. Based on the objective function values (AOT) of these evaluations, a surrogate model is fitted to the data. For this article, either a cubic radial basis function interpoland (RBFcub) or the full cubic regression polynomial (Polycubr) surrogate model is used [31].

Then, the inexpensive surrogate model is used to select a promising new sample from $\boldsymbol{h}$ to be evaluated by the expensive black-box function. If the stopping criterion, which could be a maximum number of iterations, has been reached, then the algorithm is stopped. If not, the surrogate model is updated based on the latest black-box evaluation and the search for the optimal solution is continued.

To reduce the computational time for the optimization, parallel computing is performed in MATLAB using MATLAB's Parallel Computing Toolbox. Due to the small-signal stability requirements, a very wide constraint would imply unrealistic parameter sets and an increased computational time for the optimization algorithm. Thus, for the initial optimization demonstrated in this article, the following conditions are selected for the evaluation of the expensive black-box function.

1) The SCR is set to 2.
2) The initial condition space ($V_{\text{PCC}} - \theta_{\text{PCC}}$) for basin of attraction computations is set to $V_{\text{PCC}} \in [0.8\ \ 1.2]$ p.u. and $\theta_{\text{PCC}} \in [-\pi/2\ \ \pi/2]$ with 3600 uniformly sampled points in that space.
3) The controller parameters are box-constrained as $K_{p,\text{DC0}} < K_{p,\text{DC}} < 5K_{p,\text{DC0}}$, $0.2K_{i,\text{DC0}} < K_{i,\text{DC}} < K_{i,\text{DC0}}$, $0.2K_{i,\text{PLL0}} < K_{i,\text{PLL}} < K_{i,\text{PLL0}}$, and $K_{i,\text{AC0}} < K_{i,\text{AC}} < 5K_{i,\text{AC0}}$
4) An initial condition is said to belong to the basin of attraction if the trajectory for the initial point is stable and if $i_{\max} = 1.3$ p.u., $v_{\text{dc,max}} = 1.2$ p.u., and $v_{\text{util,max}} = 1$ p.u. are not violated during the disturbance at any point in time.

The described black-box optimization algorithm is executed four times for two different surrogate models, as shown in Fig. 10. Using, the base-line design for the controller parameters from Table I for SCR $= 2$, the AOT is 103. Using the optimization algorithm for a maximum of 80 function evaluations, it takes approximately 30 min to solve, which is obviously much more acceptable compared to the brute-force grid-search approach. To that end, as it can be seen from Fig. 10, the AOT can be more than doubled in size (to around 220) by varying the controller parameters without violating any converter constraints.

$$\begin{cases} \dot{V}_{\text{PCC}} = \left(P_{\text{in}} - \frac{3}{2}\left(\frac{V_{\text{PCC}}V_g\sin(\theta_{\text{PCC}})}{X_g} + \frac{R_f}{X_g^2}f_3\right)\right)f_2 + (v_{\text{dc}} - V_{\text{dc,ref}})f_4 + (V_{\text{PCC}} - V_{\text{PCC,ref}})f_5 \\ \qquad\qquad + \sin(\theta_{\text{PCC}} - \theta_{\text{PLL}})f_6 + x_{\text{PLL}}f_7 \\ \dot{\theta}_{\text{PCC}} = \left(P_{\text{in}} - \frac{3}{2}\left(\frac{V_{\text{PCC}}V_g\sin(\theta_{\text{PCC}})}{X_g} + \frac{R_f}{X_g^2}f_3\right)\right)f_8 + (v_{\text{dc}} - V_{\text{dc,ref}})f_9 + (V_{\text{PCC}} - V_{\text{PCC,ref}})f_{10} \\ \qquad\qquad + \sin(\theta_{\text{PCC}} - \theta_{\text{PLL}})f_{11} + x_{\text{PLL}}f_{12} \\ \dot{v}_{\text{dc}} = \frac{1}{C_{\text{dc}}v_{\text{dc}}}\left(P_{\text{in}} - \frac{3}{2}\left(\frac{V_{\text{PCC}}V_g\sin(\theta_{\text{PCC}})}{X_g} + \frac{R_f}{X_g^2}f_3\right)\right) \\ \dot{\theta}_{\text{PLL}} = K_{p,\text{PLL}}V_{\text{PCC}}\sin(\theta_{\text{PCC}} - \theta_{\text{PLL}}) + K_{i,\text{PLL}}x_{\text{PLL}} \\ \dot{x}_{\text{PLL}} = V_{\text{PCC}}\sin(\theta_{\text{PCC}} - \theta_{\text{PLL}}) \end{cases} \tag{31}$$

$$f_1 = (1 + K_{p,\text{AC}}X_g\cos(\theta_{\text{PCC}} - \theta_{\text{PLL}}))^{-1}, \quad f_2 = \frac{f_1K_{p,\text{DC}}X_g\sin(\theta_{\text{PCC}} - \theta_{\text{PLL}})}{C_{\text{dc}}v_{\text{dc}}}, \quad f_3 = V_{\text{PCC}}^2 + V_g^2 - 2V_{\text{PCC}}V_g\cos(\theta_{\text{PCC}})$$

$$f_4 = K_{i,\text{DC}}X_g\sin(\theta_{\text{PCC}} - \theta_{\text{PLL}})f_1, \quad f_5 = -K_{i,\text{AC}}X_g\cos(\theta_{\text{PCC}} - \theta_{\text{PLL}})f_1, \quad f_6 = -V_{\text{PCC}}V_gK_{p,\text{PLL}}\sin(\theta_{\text{PCC}})f_1$$

$$f_7 = -V_gK_{i,\text{PLL}}\sin(\theta_{\text{PCC}})f_1,\ f_8 = \frac{K_{p,\text{DC}}X_gf_1(X_gK_{p,\text{AC}} + \cos(\theta_{\text{PCC}} - \theta_{\text{PLL}}))}{v_{\text{dc}}C_{\text{dc}}V_{\text{PCC}}}$$

$$f_9 = \frac{K_{i,\text{DC}}X_gf_1}{V_{\text{PCC}}}\left(K_{p,\text{AC}}X_g + \cos(\theta_{\text{PCC}} - \theta_{\text{PLL}})\right)$$

$$f_{10} = \frac{X_gK_{i,\text{AC}}f_1\sin(\theta_{\text{PCC}} - \theta_{\text{PLL}})}{V_{\text{PCC}}}, \quad f_{11} = f_1X_gK_{p,\text{AC}}K_{p,\text{PLL}}(V_{\text{PCC}}\cos(\theta_{\text{PCC}} - \theta_{\text{PLL}}) - V_g\cos(\theta_{\text{PLL}}))$$

$$f_{12} = K_{i,\text{PLL}}\left(1 - \frac{f_1V_g}{V_{\text{PCC}}}\left(X_gK_{p,\text{AC}}\cos(\theta_{\text{PLL}}) + \cos(\theta_{\text{PCC}})\right)\right)$$

$$\boldsymbol{x_0} = \left[V_{\text{PCC,ref}},\ \sin^{-1}\left(\frac{2P_{in}X_g}{3V_gV_{\text{PCC,ref}}}\right),\ V_{\text{dc,ref}},\ \sin^{-1}\left(\frac{2P_{in}X_g}{3V_gV_{\text{PCC,ref}}}\right),\ 0\right]^T \tag{32}$$

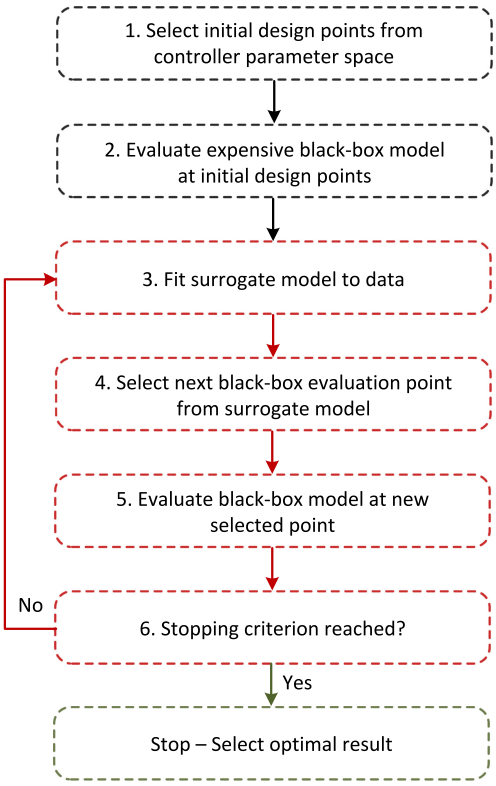

Fig. 9. Flow chart to show the steps of optimal controller parameter selection using expensive black-box optimization with a surrogate model algorithm for function fitting and evaluations of next potential optimal point.

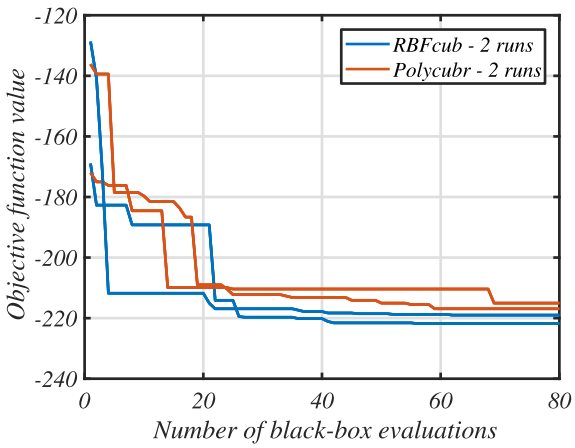

Fig. 10. Progress plot of black-box optimization using two runs of two difference surrogate models, RBFcub: cubic radial basis function interpolant, POLYcub: full cubic regression polynomial. The objective function value is the negative AOT evaluated at an initial condition set for SCR $= 2$.

Even though a particular disturbance may cause the optimized controller design to be either unstable or hit the saturation limits of the converter, it will have the lowest probability to do so, since its AOT is maximized for the specified controller parameter range. Therefore, one can say that this optimized design can lower the probability of the converter instability and, therefore, enhance the security of supply and power system reliability.

TABLE II
CONTROLLER PARAMETERS FOR OPTIMAL DESIGNS IN Fig. 10

Parameter	RBFcub 1	RBFcub 2	Polycubr 1	Polycubr 2
AOT	221.8	219	215	216.9
$K_{p,DC}$	$1.58K_{p,DC0}$	$1.58K_{p,DC0}$	$1.63K_{p,DC0}$	$1.80K_{p,DC0}$
$K_{i,DC}$	$0.2K_{i,DC0}$	$0.2K_{i,DC0}$	$0.23K_{i,DC0}$	$0.2K_{i,DC0}$
$K_{i,PLL}$	$0.2K_{i,PLL0}$	$0.2K_{i,PLL0}$	$0.33K_{i,PLL0}$	$0.2K_{i,PLL0}$
$K_{i,AC}$	$4.99K_{i,AC0}$	$4.82K_{i,AC0}$	$4.97K_{i,AC0}$	$5K_{i,AC0}$

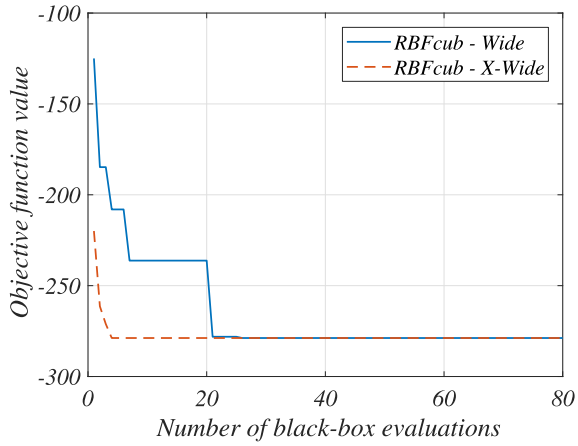

Fig. 11. Progress plot of black-box optimization using the RBFcub: cubic radial basis function interpolant surrogate model but with a wider box-constrained space for controller parameters. Wide: $K_{i,\mathrm{DC}}$ is allowed down to $0.1K_{i,\mathrm{DC0}}$. $K_{i,\mathrm{PLL}}$ is allowed down to $0.1K_{i,\mathrm{PLL0}}$. $K_{i,\mathrm{AC}}$ is allowed up to $10K_{i,\mathrm{AC0}}$. The AOT for optimized design is 278.8. The optimized controller parameters are $K_{p,\mathrm{DC}} = 1.68K_{p,\mathrm{DC0}}$, $K_{i,\mathrm{DC}} = 0.134K_{i,\mathrm{DC0}}$, $K_{i,\mathrm{PLL}} = 0.17K_{i,\mathrm{PLL0}}$, and $K_{i,\mathrm{AC}} = 9.94K_{i,\mathrm{AC0}}$. X-Wide: $K_{i,\mathrm{DC}}$ is allowed down to $0.02K_{i,\mathrm{DC0}}$. $K_{i,\mathrm{PLL}}$ is allowed down to $0.02K_{i,\mathrm{PLL0}}$. $K_{i,\mathrm{AC}}$ is allowed up to $50K_{i,\mathrm{AC0}}$. The AOT for optimized design is 278.8. The optimized controller parameters are $K_{p,\mathrm{DC}} = 1.70K_{p,\mathrm{DC0}}$, $K_{i,\mathrm{DC}} = 0.73K_{i,\mathrm{DC0}}$, $K_{i,\mathrm{PLL}} = 0.63K_{i,\mathrm{PLL0}}$, and $K_{i,\mathrm{AC}} = 21.83K_{i,\mathrm{AC0}}$.

From Table II, it can be seen that the optimal selection of all parameters except $K_{p,\mathrm{DC}}$ is at or is close to the lower or upper bounds. Therefore, it seems that the optimization is limited by the box-constrained parameter. To further verify this, $K_{i,\mathrm{DC}}$ is allowed down to $0.1K_{i,\mathrm{DC0}}$, $K_{i,\mathrm{PLL}}$ is allowed down to $0.1K_{i,\mathrm{PLL0}}$, and $K_{i,\mathrm{AC}}$ is allowed up to $10K_{i,\mathrm{AC0}}$. The optimization of this can be seen in Fig. 11. It is clear that the AOT can be further increased to 278.8 by expanding the allowed parameter space. Yet, as seen in Fig. 11, if one keeps widening the box-constrained parameter set, this does not provide a larger AOT, i.e., an optimal design can be achieved.

In addition to optimize the controller parameters, the large-signal stability of the system is largely depending on the maximum saturation parameters of the power-electronic converter. The optimized AOT using the box-constrained parameters from Fig. 10 is computed for different maximum values for dc-link voltage and converter current. These are shown in Fig. 12 where the red graph shows the change in AOT for larger maximum converter currents for a constant $V_{\mathrm{dc,max}} = 1.2$ p.u., the blue graph shows the change in AOT for increasing maximum dc-link voltage at a constant $I_{\mathrm{max}} = 1.3$ p.u., and the black dot shows the AOT for $V_{\mathrm{dc,max}} = I_{\mathrm{max}} = 1.8$ p.u. It can be observed that one can benefit much more from a larger short-term overcurrent

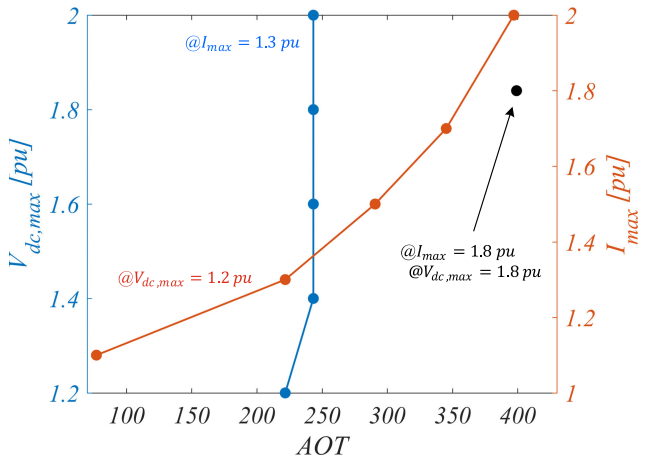

Fig. 12. Optimized area of attraction (AOT) for different maximum values for dc-link voltage and converter current. The red graph shows change in AOT for larger maximum converter currents for a constant $V_{\mathrm{dc,max}} = 1.2$ p.u. The blue graph shows the change in AOT for increasing maximum dc-link voltage at a constant $I_{\mathrm{max}} = 1.3$ p.u. The black dot shows the AOT for $V_{\mathrm{dc,max}} = I_{\mathrm{max}} = 1.8$ p.u.

contribution than from a higher voltage capability at the dc link.

V. Design Guidelines

From the numerical analysis and optimized designs, several trends are identified with the purpose to maximize the large-signal robustness of the grid-following converter system. These can be divided into an optimized design of the controller parameters, utilizing robustness associated with increased converter constraints, and by adopting short-term use of largely different controller parameters. These are shortly discussed in the following.

A. Optimized Outer-Loop Controller Parameters

From the previous section, it was shown how the outer-loop controller parameters should be selected with the aim to maximize the large-signal robustness or AOT of the system. However, besides the controller optimization during large-signal disturbances, one also has to satisfy steady-state requirements for the performance and response. For a comprehensive guideline for small-signal controller design under weak-grid conditions, see [26]. With this in mind, a general guideline for robustness toward transient stability considering the outer loops can be given as follows:

1) select $K_{p,\mathrm{DC}}$ from the black-box optimization procedure while satisfying small-signal requirements;
2) select lowest value for $K_{i,\mathrm{DC}}$ satisfying small-signal requirements;
3) select lowest value for $K_{i,\mathrm{PLL}}$ satisfying small-signal requirements;
4) select highest value for $K_{i,\mathrm{AC}}$ satisfying small-signal requirements.

B. Evaluate Value of Overcurrent Capability

In addition to the optimal selection of controller parameters, it is demonstrated that the AOT or large-signal robustness can be significantly increased by tolerating a short-term large overcurrent from the converter. For example, despite an optimized controller set, the AOT can from Fig. 12 by increased more than four times by only increasing I_{max} from 1.1 to 1.8 p.u. during short-term disturbances. Even though 1.8 p.u. seems high, this range of overcurrent capability is discussed among system operators at the moment [36]. Accordingly, realizing the advantages of an increased overcurrent contribution can be used to significantly increase the AOT. Second, it is shown that spending resources on tolerating a larger maximum dc-link voltage gives a limited increase in the AOT.

C. Consider an Event-Driven Controller Design

When comparing the optimized controller parameters for large-signal robustness, there may be a large difference between these and what can be allowed from a steady-state small-signal point of view. Therefore, it may be beneficial to allow for an event-driven selection of outer-loop parameters such that the optimized design can be utilized whenever needed. For example, allowing a large change in the parameters under large-signal disturbances where the state variables deviate sufficiently from their references or when, e.g., a low SCR condition is detected. Such methods will not be further detailed here but may be implemented similarly to proposals utilizing an event-driven controller [37]–[39] or adaptive controller structure [13].

VI. Experimental Results

All observed stability trends and optimized area of attraction designs from the previous sections are based on the validity of the reduced-order model in (31). Therefore, this model is compared against experimental results obtained from a low-power back-to-back converter setup. The experimental setup uses a 15 kVA, 400 V system, where all other parameters are scaled to this power and voltage base from the wind turbine parameters in Table I. The switching frequency is 10 kHz and the inner-loop bandwidth is 500 Hz, which supports the matching results. The experimental setup uses an Imperix hardware setup with two three-phase converters configured in a back-to-back configuration. One converter is controlled to feed in a reference active power to the dc-link and the other operates as the grid-connected converter shown in Fig. 1.

The converters are build from Imperix PEB 8024 silicon carbide power modules. The dc-link capacitance is measured to be 730 μF and the converter control is implemented using the Imperix B-BOX RCP 3.0 for rapid control prototyping of power electronic systems. A digitally controlled relay is used to connect and disconnect a parallel inductive branch with 3 mH. In the main branch, the inductance is manually selected as either 18 mH or 19 mH. Thus, when the relay is connected,

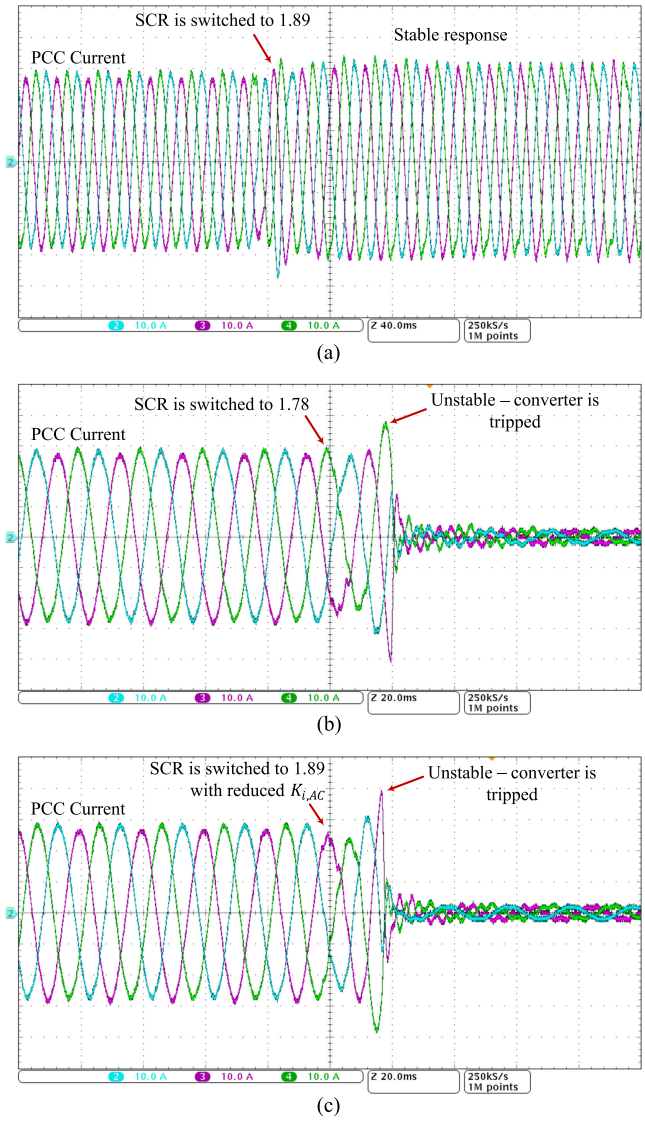

Fig. 13. PCC current of grid-connected converter under different impedance switchings. (a) SCR is switched from 11 to 1.89, resulting in a stable response. (b) SCR is switched from 11 to 1.78, resulting in an unstable response. (c) SCR is switched from 11 to 1.89 but with a reduced $K_{i,\mathrm{AC}}$, which is sufficient to trigger instability. For all results the experimental setup is operated at 0.85 p.u. active power transfer.

the large reactance is connected in parallel with a 3 mH inductor, resulting in a high SCR around 11. When the relay is disconnected, the equivalent reactance increases and the SCR decreases to 1.89 or 1.78 (18 or 19 mH). Impedance jumps and an input power step is used to verify the reduced-order large-signal model.

As seen in Fig. 13(a), when the SCR is switched to 1.89, the system stands stable. When the SCR is further reduced to 1.78 in Fig. 13(b), the system becomes unstable and the converter is tripped. To that end, when the SCR is switched to 1.89 but with a reduced $K_{i,\mathrm{AC}} = 0.25K_{i,\mathrm{AC0}}$, then the system loses stability. This clearly supports the trend observed that an increased $K_{i,\mathrm{AC}}$ provides a higher large-signal robustness. These three tests were also conducted using the reduced-order model. Here, the system

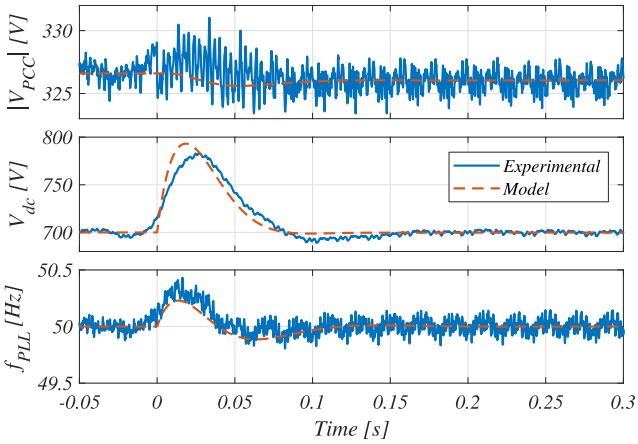

Fig. 14. Comparison between experimental setup and the reduced-order model for a step active power increase from 0.25 to 0.75 p.u. The PCC voltage magnitude, dc-link voltage and PLL estimated frequency are compared and shown.

is unstable when SCR $= 1.78$, as seen in Fig. 13(b) and it is stable for SCR down to 1.89. Also, when the SCR is switched to 1.89 but with a reduced $K_{i,\mathrm{AC}}$, as done in Fig. 13(c), the system loses stability. Accordingly, it is seen that the experimental test results well match the stability predictions of the reduced-order model.

In addition to this, an input power step response is performed in the laboratory and the responses of the state variables are recorded. This is shown in Fig. 14 where the measured experimental results are compared to the results from the reduced-order model. As previously seen, the obtained results match well the reduced-order model. This is despite that noise and measurement inaccuracies are pronounced for the experimental setup.

VII. Conclusion

To expand upon the knowledge of the large-signal performance and stability of grid-following converters, this work analyzes the stability and robustness during high-impedance grid-disturbances. A reduced-order large-signal model is developed and analyzed using the AOT as a measure for large-signal robustness. Through a surrogate-model expensive black-box optimization algorithm, a computational-efficient optimal design of the outer-loop controller parameters has been given. Based on these, a design guideline for outer-loop control is proposed to maximize the large-signal robustness of the system. It is disclosed that one should seek to minimize the integral gains of the dc-link control and the PLL whereas, one should seek to maximize the integral gain of the ac-side voltage control. To that end, it is shown that the large-signal robustness can be significantly increased by allowing for a larger short-term converter overcurrent capability. Along these lines, it is shown that a higher overvoltage capability at the dc-link does not provide any significant advantages compared to a larger overcurrent capability. Finally, the reduced-order large-signal model, from where all analyses and trends are disclosed, is verified using an experimental test setup.

REFERENCES

[1] B. Kroposki *et al.*, "Achieving a 100 % renewable grid: Operating electric power systems with extremely high levels of variable renewable energy," *IEEE Power Energy Mag.*, vol. 15, no. 2, pp. 61–73, Mar. 2017.

[2] Ö. Göksu, R. Teodorescu, C. L. Bak, F. Iov, and P. C. Kjær, "Instability of wind turbine converters during current injection to low voltage grid faults and PLL frequency based stability solution," *IEEE Trans. Power Syst.*, vol. 29, no. 4, pp. 1683–1691, Jul. 2014.

[3] D. Dong, B. Wen, D. Boroyevich, P. Mattavelli, and Y. Xue, "Analysis of phase-locked loop low-frequency stability in three-phase grid-connected power converters considering impedance interactions," *IEEE Trans. Ind. Electron.*, vol. 62, no. 1, pp. 310–321, Jan. 2015.

[4] M. G. Taul, X. Wang, P. Davari, and F. Blaabjerg, "An overview of assessment methods for synchronization stability of grid-connected converters under severe symmetrical grid faults," *IEEE Trans. Power Electron.*, vol. 34, no. 10, pp. 9655–9670, Oct. 2019.

[5] NationalGrid, "Performance of phase-locked loop based converters," NationalGrid, London, U.K., Tech. Rep., 2017.

[6] X. Wang, M. G. Taul, H. Wu, Y. Liao, F. Blaabjerg, and L. Harnefors, "Grid-synchronization stability of converter-based resources-an overview," *IEEE Open J. Ind. Appl.*, vol. 1, pp. 115–134, 2020.

[7] I. Erlich, F. Shewarega, S. Engelhardt, J. Kretschmann, J. Fortmann, and F. Koch, "Effect of wind turbine output current during faults on grid voltage and the transient stability of wind parks," in *Proc. IEEE Power Energy Soc. General Meeting*, Jul. 2009, pp. 1–8.

[8] X. He, H. Geng, and G. Yang, "Synchronization stability analysis of grid-tied power converters under severe grid voltage sags," in *Proc. IEEE Int. Power Electron. Appl. Conf. Expo.*, Nov. 2018, pp. 1–6.

[9] M. G. Taul, X. Wang, P. Davari, and F. Blaabjerg, "An efficient reduced-order model for studying synchronization stability of grid-following converters during grid faults," in *Proc. 20th Workshop Control Model. Power Electron.*, Jun. 2019, pp. 1–7.

[10] Q. Hu, L. Fu, F. Ma, and F. Ji, "Large signal synchronizing instability of PLL-based VSC connected to weak AC grid," *IEEE Trans. Power Syst.*, vol. 34, no. 4, pp. 3220–3229, Jul. 2019.

[11] W. Wang *et al.*, "Instability of PLL-synchronized converter-based generators in low short-circuit systems and the limitations of positive sequence modeling," in *Proc. IEEE North Amer. Power Symp.*, Sep. 2018, pp. 1–6.

[12] Q. Hu, J. Hu, H. Yuan, H. Tang, and Y. Li, "Synchronizing stability of DFIG-based wind turbines attached to weak AC grid," in *Proc. IEEE 17th Int. Conf. Elect. Mach. Syst.*, Oct. 2014, pp. 2618–2624.

[13] H. Wu and X. Wang, "Design-oriented transient stability analysis of PLL-synchronized voltage-source converters," *IEEE Trans. Power Electron.*, vol. 35, no. 4, pp. 3573–3589, Apr. 2020.

[14] M. G. Taul, X. Wang, P. Davari, and F. Blaabjerg, "Robust fault ride through of converter-based generation during severe faults with phase jumps," *IEEE Trans. Ind. Appl.*, vol. 56, no. 1, pp. 570–583, Jan. 2020.

[15] H. Geng, L. Liu, and R. Li, "Synchronization and reactive current support of PMSG-based wind farm during severe grid fault," *IEEE Trans. Sustain. Energy*, vol. 9, no. 4, pp. 1596–1604, Oct. 2018.

[16] S. Ma, H. Geng, L. Liu, G. Yang, and B. C. Pal, "Grid-synchronization stability improvement of large scale wind farm during severe grid fault," *IEEE Trans. Power Syst.*, vol. 33, no. 1, pp. 216–226, Jan. 2018.

[17] X. He, H. Geng, R. Li, and B. C. Pal, "Transient stability analysis and enhancement of renewable energy conversion system during LVRT," *IEEE Trans. Sustain. Energy*, vol. 11, no. 3, pp. 1612–1623, Jul. 2020.

[18] H. Wu and X. Wang, "An adaptive phase-locked loop for the transient stability enhancement of grid-connected voltage source converters," in *Proc. IEEE Energy Convers. Congr. Expo.*, Sep. 2018, pp. 5892–5898.

[19] M. G. Taul, R. E. Betz, and F. Blaabjerg, "Rapid impedance estimation algorithm for mitigation of synchronization instability of paralleled converters under grid faults," in *Proc. IEEE 22nd Eur. Conf. Power Electron. Appl.*, Sep. 2020, pp. 1–5.

[20] H. Wu and X. Wang, "Design-oriented transient stability analysis of grid-connected converters with power synchronization control," *IEEE Trans. Ind. Electron.*, vol. 66, no. 8, pp. 6473–6482, Aug. 2019.

[21] M. G. Taul, X. Wang, P. Davari, and F. Blaabjerg, "Systematic approach for transient stability evaluation of grid-tied converters during power system faults," in *Proc. IEEE Energy Convers. Congr. Expo.*, Sep. 2019, pp. 5191–5198.

[22] M. G. Taul, S. Golestan, X. Wang, P. Davari, and F. Blaabjerg, "Modeling of converter synchronization stability under grid faults: The general case," *IEEE J. Emerg. Sel. Topics Power Electron.*, early access, 2020.

[23] D. Dong, B. Wen, P. Mattavelli, D. Boroyevich, and Y. Xue, "Grid-synchronization modeling and its stability analysis for multi-paralleled three-phase inverter systems," in *Proc. 28th Annu. IEEE Appl. Power Electron. Conf. Expo.*, Mar. 2013, pp. 439–446.

[24] M. G. Taul, X. Wang, P. Davari, and F. Blaabjerg, "Reduced-order and aggregated modeling of large-signal synchronization stability for multi-converter systems," *IEEE J. Emerg. Sel. Topics Power Electron.*, early access, 2020.

[25] J. Zhao, M. Huang, and X. Zha, "Transient stability analysis of grid-connected VSIS via PLL interaction," in *Proc. IEEE Int. Power Electron. Appl. Conf. Expo.*, Nov. 2018, pp. 1–6.

[26] J. F. Morris, K. H. Ahmed, and A. Egea-Alvarez, "Analysis of controller bandwidth interactions for vector-controlled VSC connected to very weak AC grids," *IEEE J. Emerg. Sel. Topics Power Electron.*, early access, 2020.

[27] Z. Yang, R. Ma, S. Cheng, and M. Zhan, "Nonlinear modeling and analysis of grid-connected voltage source converters under voltage dips," *IEEE J. Emerg. Sel. Topics Power Electron.*, vol. 8, no. 4, pp. 3281–3292, Dec. 2020.

[28] M. Huang, S. Wong, C. K. Tse, and X. Ruan, "Catastrophic bifurcation in three-phase voltage-source converters," *IEEE Trans. Circuits Syst. I. Regular Paper*, vol. 60, no. 4, pp. 1062–1071, Apr. 2013.

[29] M. Huang, Y. Peng, C. K. Tse, Y. Liu, J. Sun, and X. Zha, "Bifurcation and large-signal stability analysis of three-phase voltage source converter under grid voltage dips," *IEEE Trans. Power Electron.*, vol. 32, no. 11, pp. 8868–8879, Nov. 2017.

[30] L. Harnefors, A. G. Yepes, A. Vidal, and J. Doval-Gandoy, "Passivity-based controller design of grid-connected VSCs for prevention of electrical resonance instability," *IEEE Trans. Ind. Electron.*, vol. 62, no. 2, pp. 702–710, Feb. 2015.

[31] J. Müller, "MATSuMoTo: The MATLAB surrogate model toolbox for computationally expensive black-box global optimization problems," 2014, *arXiv:1404.4261*.

[32] J. Müller and R. Piché, "Mixture surrogate models based on Dempster-Shafer theory for global optimization problems," *J. Global Optim.*, vol. 51, no. 1, pp. 79–104, 2011.

[33] J. Müller, C. A. Shoemaker, and R. Piché, "SO-MI: A surrogate model algorithm for computationally expensive nonlinear mixed-integer black-box global optimization problems," *Comput. Oper. Res.*, vol. 40, no. 5, pp. 1383–1400, 2013.

[34] J. Müller, C. A. Shoemaker, and R. Piché, "SO-I: A surrogate model algorithm for expensive nonlinear integer programming problems including global optimization applications," *J. Global Optim.*, vol. 59, no. 4, pp. 865–889, 2013.

[35] J. Müller and C. A. Shoemaker, "Influence of ensemble surrogate models and sampling strategy on the solution quality of algorithms for computationally expensive black-box global optimization problems," *J. Global Optim.*, vol. 60, no. 2, pp. 123–144, 2014.

[36] NationalGrid, *Draft grid code—Grid forming converter specification*, 2020. [Online]. Available: https://www.nationalgrideso.com/document/159296/download.

[37] W. P. M. H. Heemels, K. H. Johansson, and P. Tabuada, "An introduction to event-triggered and self-triggered control," in *Proc. IEEE 51st IEEE Conf. Decis. Control*, 2012, pp. 3270–3285.

[38] N. Mohammed, T. Kerekes, and M. Ciobotaru, "An online event-based grid impedance estimation technique using grid-connected inverters," *IEEE Trans. Power Electron.*, vol. 36, no. 5, pp. 6106–6117, May 2021.

[39] S. Sahoo, T. Dragičević, and F. Blaabjerg, "An event-driven resilient control strategy for dc microgrids," *IEEE Trans. Power Electron.*, vol. 35, no. 12, pp. 13 714–13 724, Dec. 2020.

Mads Graungaard Taul (Member, IEEE) received the B.Sc. and M.Sc. degrees in electrical energy engineering with a specialization in power electronics and drives in 2016 and 2019, respectively, and the Ph.D. degree in power electronic systems from Aalborg University, Aalborg, Denmark, in 2020.

He was a Visiting Researcher with the Department of Electrical Engineering and Computer Science, University of California, Berkeley, Berkeley, CA, USA, from August 2019 to January 2020 and a Postdoctoral Researcher with the Department of Energy Technology, Aalborg University, Aalborg, Denmark, in 2020. He is currently a Power System Engineer with Energinet, ErritsØ, Denmark.

Dr. Taul, in connection with his M.Sc. degree, was the recipient of the First Prize Master's Thesis Award for Excellent and Innovative Project Work by the Energy Sponsor Programme.

Chao Wu (Member, IEEE) was born in Hubei Province, China. He received the B.Eng. degree in electrical engineering from the HeFei University of Technology, Hefei, China, in 2014, and the Ph.D. degree in electrical engineering from Zhejiang University, Hangzhou, China, in 2019.

He is currently a Postdoctoral Researcher with the Department of Energy Technology, Aalborg University, Aalborg, Denmark. His current research interests include cooperative control of multiconverter systems, particularly the control and operation of doubly fed induction generators for dc connection and the transient stability of power converters.

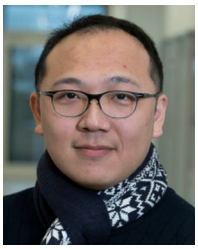

Shih-Feng Chou (Member, IEEE) received the B.S. and M.S. degrees in electrical engineering from National Tsing Hua University, Hsinchu, Taiwan, in 2009 and 2011, respectively. He is currently working toward the Ph.D. degree with Aalborg University, Aalborg, Denmark.

He had performed R&D in power electronics for renewable energy systems with Delta Electronics, Inc., Taoyuan, Taiwan, from 2012 to 2017. Since 2017, he has been a Research Assistant with the Department of Energy Technology, Aalborg University. His research focuses on modeling of large-scale power-electronics-based power system.

Frede Blaabjerg (Fellow, IEEE) received the Ph.D. degree in electrical engineering from Aalborg University, Aalborg, Denmark, in 1995.

He was with the ABB-Scandia, Randers, Denmark, from 1987 to 1988. He became an Assistant Professor in 1992, an Associate Professor in 1996, and a Full Professor of Power Electronics and Drives in 1998. From 2017, he became a Villum Investigator. He has authored or coauthored more than 600 journal papers in the fields of power electronics and its applications. He is the co-author of four monographs and editor of ten books in power electronics and its applications. His current research interests include power electronics and its applications such as in wind turbines, PV systems, reliability, harmonics, and adjustable speed drives.

Dr. Blaabjerg was recipient of 33 IEEE Prize Paper Awards, the IEEE PELS Distinguished Service Award in 2009, the EPE-PEMC Council Award in 2010, the IEEE William E. Newell Power Electronics Award 2014, the Villum Kann Rasmussen Research Award 2014, the Global Energy Prize in 2019, and the 2020 IEEE Edison Medal. He was the Editor-in-Chief of the IEEE TRANSACTIONS ON POWER ELECTRONICS from 2006 to 2012. He has been Distinguished Lecturer for the IEEE Power Electronics Society from 2005 to 2007 and for the IEEE Industry Applications Society from 2010 to 2011 as well as from 2017 to 2018. In 2019–2020, he was a President of IEEE Power Electronics Society. He has been Vice-President of the Danish Academy of Technical Sciences. He is honoris causa with University Politehnica Timisoara (UPT), Timişoara, Romania and with Tallinn Technical University, Tallinn, Estonia. He is nominated in 2014–2020 by Thomson Reuters to be between the 250 most-cited researchers in engineering in the world.